Journal of Marine Research, 56, 295–328, 1998

Journal of
MARINE RESEARCH

Volume 56, Number 2

Topography and barotropic transport control by bottom friction

by William K. Dewar[1]

ABSTRACT

The problem of the stratified general circulation in the presence of topography is revisited. The novel effect examined here is that of localized, but large-scale, topographic anomalies on the wind-driven circulation, a problem whose relevance is found in the occurrence of many such features in the open ocean. Using the classical methods of homogenization theory, it is argued that the barotropic transport near topography can come under the direct control of bottom friction. This result differs substantively from either the well-known Sverdrup constraint (which applies to a flat-bottomed ocean, or to one with a resting deep layer) or its recent extensions that allow for planar bottom topographic profiles.

Bottom friction emerges as a controlling parameter roughly in the event that the topography forms closed $f/(H - h_b)$ contours, where $H - h_b$ is the total fluid depth, although the theoretical minimum requirements are somewhat looser than this. Our analytical predictions are supported by numerical experimentation with a multi-layer quasi-geostrophic model, and we examine some mean flow observations from the North and South Atlantic in light of the theory. In particular, the theory can rationalize the 100 Sv transport observed recently around the Zapiola Drift.

1. Introduction

The linear vorticity equation

$$\beta v = f w_z \tag{1.1}$$

where β is the meridional gradient of the Coriolis parameter f, v is meridional velocity, w is vertical velocity and the subscript z denotes differentiation with respect to depth, is the

1. Department of Oceanography and Supercomputer Computations Research Institute, Florida State University, Tallahassee, Florida, 32306, U.S.A.

cornerstone of large-scale dynamics. Sverdrup (1947) exploited (1.1) to obtain his famous constraint on the net meridional transport; namely

$$\beta \int_{z_0}^{0} v\,dz = f w_e \tag{1.2}$$

where w_e represents Ekman pumping and z_0 a depth beyond which motion is assumed to vanish. (Note that (1.2) also holds if the ocean has a flat bottom and bottom Ekman layers are neglected.) The so-called Sverdrup relation in (1.2) has had a significant effect on theoretical developments in large-scale ocean dynamics, in that most models of stratified general circulation assume a Sverdrup constraint (Rhines and Young, 1982a,b; Luyten et al., 1983). Note, however, that if the ocean bottom is not flat, as is typical of all oceans, and if deep flows are nontrivial, as seems often to be the case, bottom vertical velocities can contribute to (1.2) and break the connection between Ekman pumping and barotropic transport. The impact of this on the wind-driven circulation is not well understood.

Here, we analyze the structure of the general circulation in the presence of topography, and derive the conditions under which (1.2) is not valid. These conditions are met in the open ocean, and we propose a general circulation theory which allows for them. Our results argue that bottom friction plays an important role in controlling transport in the presence of topographic anomalies and North and South Atlantic observations are suggestive of the relevance of this idea.

a. Background

Wunsch and Roemmich (1985; hereafter WR) argued that an earlier North Atlantic circulation scheme proposed by Leetmaa et al. (1977), which was consistent with (1.2) and closed in the upper 1 km, resulted in a heat flux too small by an order of magnitude to be reconciled with other estimates. They suggested the North Atlantic thermohaline cell was missing from that scheme, a feature whose inclusion modifies (1.2) to:

$$\beta \int_{-(H-h_b)}^{0} v\,dz = f(w_e - w_b) = f(w_e - \mathbf{u}_b \cdot \nabla h_b) \tag{1.3}$$

where $\mathbf{u}_b$ is horizontal bottom velocity, $H - h_b$ represents the variable ocean depth and bottom vertical velocity, w_b, is computed using "topographic deflection." The applicability of (1.2) to the North Atlantic was thus seriously challenged.

i. Atlantic observations. The formula in (1.3) presupposes a knowledge of oceanic bathymetry. The main topographic features of the Atlantic basin are the Mid-Atlantic Ridge (MAR) and the continental rises on the meridional basin edges (see Fig. 1). Of particular importance for this work are the South Atlantic feature known as the Zapiola Drift (ZD in Fig. 1) and the North Atlantic MAR anomaly known as the Azores Plateau (AP in Fig. 1).

The AP appears as a local topographic high of roughly 1200 m amplitude relative to the MAR, and a lateral extent of 1500 km in both the meridional and zonal directions. The

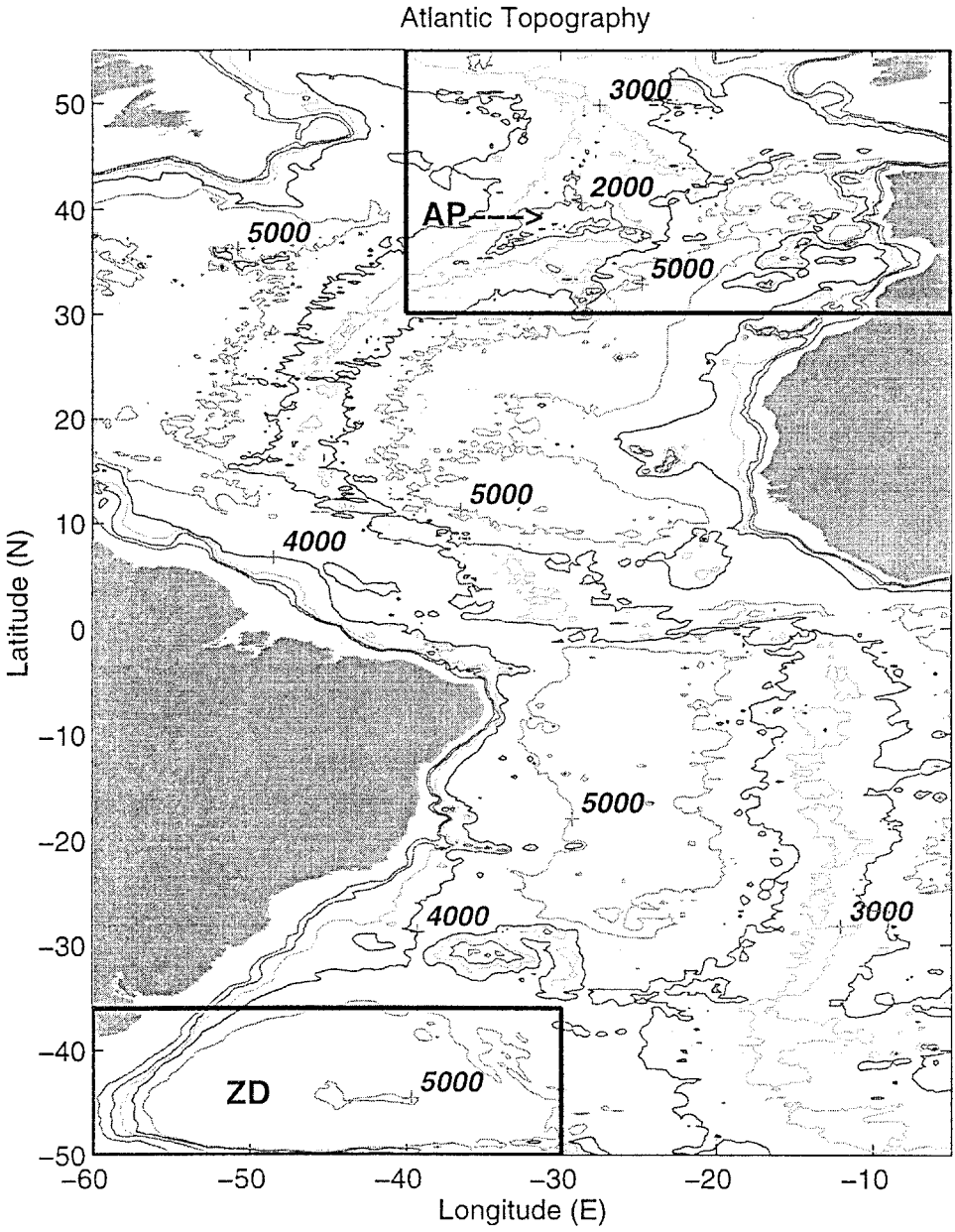

Figure 1. Atlantic topography. Smoothed ETOPO-5 data, subsampled at ¼° resolution, is contoured to show the Atlantic bottom topography. The main features include the Mid-Atlantic Ridge (MAR) and continental slopes. The Azores Plateau is labeled AP and the Zapiola Drift ZD. The boxed areas denote the areas displayed in Figure 2. CI = 1000 m.

Zapiola Drift (ZD hereafter) is a depositional bottom feature, the outline of which appears in the 4000 m and 5000 m contours in Figure 1. Transects across it reveal that it is roughly 1200 m in amplitude, reaching from a deepest point of 6000 m on its west and peaking at roughly 4800 m near (45S, 42W). It is also roughly 1500 km in both zonal and meridional extent.

Evidence has accumulated in the last decade that mean flows are often found in the vicinity of these topographic features. For example, Pollard et al. (1996) argue based on CTD and Sea Soar data that the flow in the vicinity of the AP involves two anticyclonic gyres (relative to 2000 m) of between 5 and 15 Sv (Sv $= 10^6$ m^3 s^{-1}). The westernmost of these is centered on (42N, 27W), just north of the Azores Islands. Klein and Siedler (1989) show several examples of gyres over the AP. The clearest example comes from their summer estimates and consists of a 1.5 Sv (relative to 800 m) anticyclonic gyre over the AP. They also find no clear signal in the vicinity of the eastern Pollard gyre and a cyclonic gyre closer to the Mediterranean outflow. Hydrographic surveys reported by Kraus and Kase (1984) show a high pressure center over the AP and subsequent float releases (drogued at 100 m) moved anticyclonically around the AP. Lozier et al. (1995) present a streamfunction on their $\sigma_{1000} = 31.85$ surface which shows a local ridge of high pressure ending over the AP. Sy (1988) performed an inverse analysis of the TOPOGULF hydrographic data and found an anticyclonic circulation on the eastern side of the AP, with a relevant flow signature extending to the bottom.

Some remarkable observations have also been obtained in the vicinity of the ZD. Combining ADCP and hydrographic data, Saunders and King (1995a,b) convincingly inferred the presence of anticyclonic bottom flow in the vicinity of the Zapiola Drift. The velocity amplitude was 0 (10 cm s^{-1}) at the bottom and the associated transport was in excess of 100 Sv. These very dramatic observations are also consistent with current meter records (Weatherly, 1993) and geological evidence (Flood and Shor, 1988), both of which support the persistence of the Zapiola Anticyclone.

It is tempting to suggest a connection between these topographic anomalies and the observed flows. This, and the size of the flows (100 Sv for the Zapiola Anticyclone), provide the principal motivation for this work. A secondary motivation comes from the possible climatic roles of these anticyclones. For example, McCartney (1996, pers. communication) cites the Lozier et al. (1995) streamfunction as evidence that the saline influence of the Mediterranean outflow is not spread along the eastern edge of the North Atlantic, as has been classically postulated. Instead, he argues that the Mediterranean salt follows an open ocean route to the North Atlantic Current (NAC), a path necessarily involving a mid-ocean anticyclonic circulation. (For this mechanism to function the anticyclone must be active at least to 1500 m depth.) This is of climatic significance, as the salinity of the NAC is central to the production of North Atlantic Deep Water. The ZD stands between the open Atlantic and the Antarctic Circumpolar Current at the southern end of the Argentine Basin. As discussed by Saunders and King (1995b), the Zapiola Anticyclone impacts tracer transport estimates.

ii. Previous modeling studies. A barotropic ocean yields the simplest dynamical model incorporating topography. In this case, the flow is governed by

$$J\left(P, \beta y - \frac{f_o h_b}{H}\right) = \frac{f_o^2}{H}\left(w_e - \frac{\delta_e}{f_o}\nabla^2 P\right) \tag{1.4}$$

where P is pressure, H is the average fluid depth, h_b represents topography, J denotes the usual Jacobian operator and δ_e is bottom Ekman layer depth. The quantity $q = \beta y - (f_o h_b/H)$ in (1.4) is the quasi-geostrophic approximation of $f/(H - h_b)$, the planetary potential vorticity.

Eq. (1.4) draws attention to $f/(H - h_b)$ because of its role in determining the barotropic general circulation. One such map for the North Atlantic appears in Figure 2a along with an estimate of the zero wind stress curl line. Figure 2b displays $f/(H - h_b)$ for the South Atlantic in the vicinity of the Zapiola Drift. Most of the $f/(H - h_b)$ contours strike lateral boundaries; solving for P by integration along these contours is straightforward, given an Ekman pumping field (Koblinsky, 1990). The AP and the ZD are, however, characterized by closed $f/(H - h_b)$ contours, and in such areas, the above approach fails. Welander (1968) and Young (1981) argued that the streamfunction amplitude in such areas is governed by bottom friction. The analysis in Young (1981) depended upon an area integration of (1.4) over a closed $f/(H - h_b)$ contour, which yields

$$\iint w_e \, dA = \frac{\delta_e}{f_o}\oint \nabla P \cdot \hat{n} dl \tag{1.5}$$

where the line integral is performed on the bounding contour, demonstrating P is inversely proportional to δ_e. In essence, the flow accelerates to the point that lateral fluxes in the bottom Ekman layer balance the mass fluxes out of the upper wind-driven Ekman layer. The quantity P can thus be computed from (1.5) and the complete solution of (1.4) for arbitrary topography can be obtained.

Two important early attempts to generalize the barotropic model to include stratification and topography were the nearly simultaneous studies of DeSzoeke (1985; DS hereafter) and Cessi and Pedlosky (1986; CP hereafter). Both studies used the methods of Rhines and Young (1982a,b) to compute the general circulation structure in the presence of sloping bottom topographies. DS forwarded an extended Sverdrup formula appropriate to this case and CP argued that topography generally forced internal jets into the circulation. Implicit in both studies is the assumption that the wind-driven flow is itself strong enough to penetrate to the ocean floor.

More recent studies by Salmon (1992), Becker (1995) and Thompson (1995) have focused on the role of continental slopes and their natural tendency to drive layer thicknesses to small values. The role of topographically closed geostrophic contours in the lower layer was emphasized in the latter, both for steady and spin-up models. Mid-ocean topographic anomalies have also been examined for the roles they might play in controlling

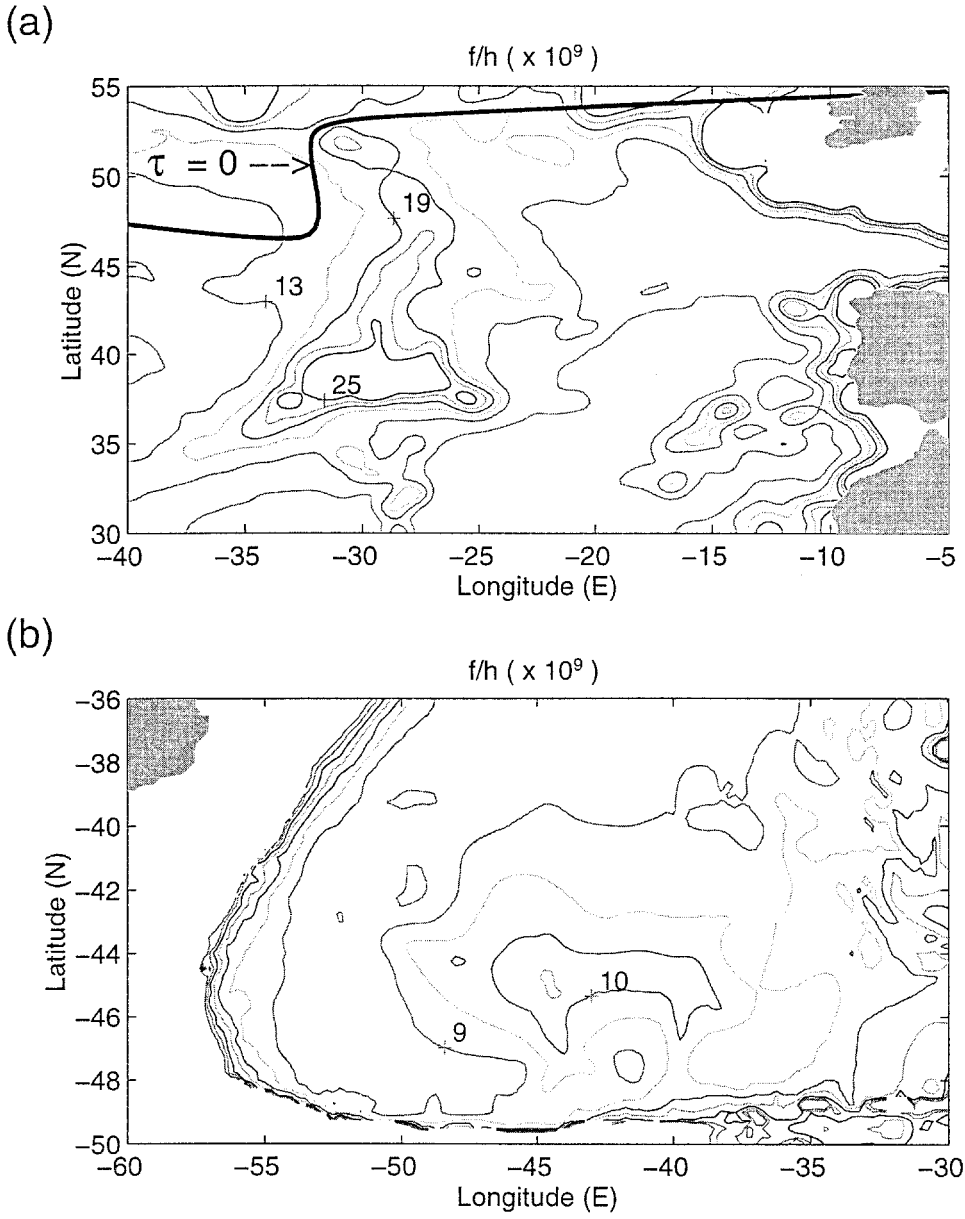

Figure 2. Barotropic potential vorticity. The Azores Plateau area appears in (a); the Zapiola Drift area appears in (b). The ETOPO-5 data have been smoothed in (a) and $f/(H - h_b)$ is plotted. Raw depth data are used in (b). The solid line in (a) denotes the zero wind stress curl line. Note the $0(1000\ \text{km})^2$ closed contours in both cases. CI = $.5 \times 10^{-9}\ \text{s}^{-1}$ for the ZD, and $3 \times 10^{-9}\ \text{s}^{-1}$ for the AP.

thermohaline flow (Rhines, 1989; Kawase and Straub, 1991; Kawase, 1993). Marshall (1995a) calculated the wind-driven structure in the presence of arbitrary topography. In his theory, topography did not impact the circulation unless it penetrated the base of the wind-driven flow. He computed the sense of the circulation around topographic anomalies in a continuously stratified fluid and further considered application to the Antarctic Circumpolar Current (Marshall, 1995b).

b. This paper

In spite of the attention that topography has received in the study of the stratified wind-driven circulation, the impact of localized topography remains poorly understood. The study of such topography forms the main focus of this paper. Oceanic motivation comes from the maps in Figure 2 and the observations described earlier.

The present study complements the DS and CP analyses by considering the wind-driven circulation in a regime where it is incapable on its own of penetrating to the bottom. Parameter estimation suggests the need for such a theory. We nonetheless allow for the possibility that the deep flow is in motion, a point which contrasts the present study with that of Marshall (1995a). Finally, our focus is on mid-ocean anomalies rather than the continental rise topography which constituted much of the focus of Thompson (1995).

Accordingly, we find that localized topographic anomalies are generally associated with regions of anomalous general circulation dynamics. In such regions, bottom friction can play a central role in governing the large-scale response. A classic Sverdrup flow results if bottom friction is strong relative to eddy stirring. The opposing limit of weak bottom friction yields a result much like that of Welander; namely, the transport is inversely proportional to bottom friction. The present theory complements Welander (1968) by clarifying how the transport is partitioned in the vertical and how it is affected by stratification. This latter limit represents a considerable dynamical departure from the Sverdrup case, in which the bottom friction fails to appear. Reasonable estimates suggest the real ocean lies in between the limits of weak and strong bottom friction, and can exhibit the behavior of the former category. Bottom friction has a major role to play in both cases in setting the transport amplitude. Finally, we suggest these ideas explain the apparent transport differences between the AP and the ZD.

The theory is advanced in Section 2 by examination of an analytical two-layer, large-scale, quasi-geostrophic model. Numerical experiments using a three-layer full quasi-geostrophic model are discussed in Section 3 and the paper closes with a conclusions and discussion section. An analytical three-layer model is discussed in an Appendix.

2. An analytical two-layer model

We first consider a two-layer system (refer to the three-layer schematic in Fig. 3) and for simplicity restrict the model to the large-scale, steady quasi-geostrophic regime. The

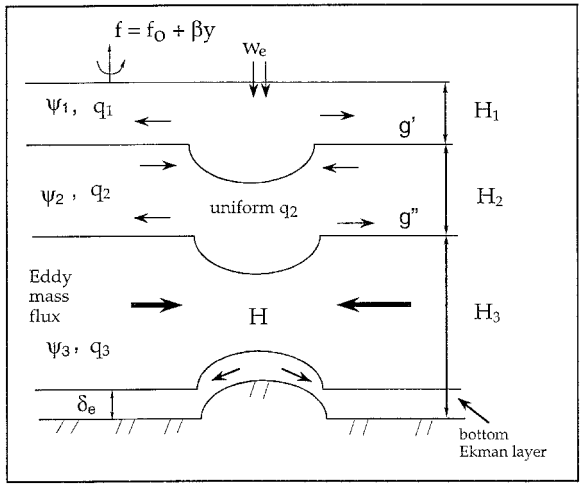

Figure 3. Model schematic and analytical model dynamics. A three-layer schematic appears; suppression of the middle layer yields the two-layer model of Section 2. The arrows in each layer denote eddy mass flux. In the case where the upper layer develops closed zones, the net Ekman pumping must be balanced by an eddy-driven mass flux. For a downwelling, this requires a local thickness maximum. That thermocline topography is imprinted through the second layer and onto the lower layer. The resulting eddy-driven flow, which attempts to mix potential vorticity downgradient, accelerates until balanced by bottom drag.

dimensional equations governing the two layers are:

$$J(\psi_1, q_1) = \frac{f_o w_e}{H_1} + R\nabla^2 q_1, \qquad q_1 = \beta y + \frac{f_o^2}{g' H_1}(\psi_2 - \psi_1) \tag{2.1a}$$

$$J(\psi_2, q_2) = R\nabla^2 q_2 - D\nabla^2 \psi_2, \qquad q_2 = \beta y + \frac{f_o^2}{g' H_2}(\psi_1 - \psi_2) + \frac{f_o}{H_2} h_b \tag{2.1b}$$

and represent the large-scale potential vorticity dynamics of each layer (see CP). The quantities ψ_1, ψ_2 denote the transport streamfunction in layers 1 and 2, respectively. The environmental parameters f_o, β, g', H_1 and H_2 represent the Coriolis parameter, beta parameter, reduced gravity associated with the inter-layer density difference ($g' = g(\rho_2 - \rho_1)/\rho_0$) and upper and lower layer thickness. The Jacobian operator is denoted by the J, h_b represents the bottom topography and the system is forced by the Ekman pumping field w_e.

The most important dynamical simplification in (2.1) is the elimination of relative vorticity from potential vorticity. An eddy parameterization is thus required and appears in (2.1) as the diffusion of potential vorticity with coefficient R. Such a parameterization, meant to represent the effects of baroclinic instability, is at the heart of many analytical general circulation models (Rhines and Young, 1982a,b) and is related to the downgradient thickness diffusion parameterization recently advanced by Gent and McWilliams (1990) for use in noneddy-resolving numerical models.

The parameterization of eddies in the presence of topography is the subject of considerable modern debate. Holloway (1992) recommends relaxing models toward maximum entropy states. Thompson (1995) uses an interface diffusion in place of q diffusion, a parameterization like that employed by Rhines (1989). We proceed here with q diffusion because this permits considerable analytical progress and demonstrates some novel roles for topography in the general circulation. We argue later that this parameterization, at worst, does no qualitative harm. Some results suggest it is quantitatively accurate for our purposes.

Finally, bottom friction, representing an Ekman pumping out of the bottom boundary layer, appears in (2.1) and is proportional to D. In terms of Ekman layer theory, this is:

$$D = \frac{\delta_e f_o}{H_2} = \sqrt{\frac{A_v}{f_o}}\frac{f_o}{H_2} \tag{2.2}$$

where the Ekman layer depth, δ_e, is typically 10 m, implying an A_v of 10^2 cm^2 s^{-1}.

We consider the solution of (2.1) in a closed rectangular domain. No normal flow boundary conditions are used, the domain extends from $-L$ to L meridionally and zonally from x_w to x_e. The point (0, 0) is assumed to lie within the basin. Also, for purposes of this calculation, we will employ the analytically convenient topographic form

$$\begin{aligned} h_b(x, y) &= h_{bo}\left(1 - \frac{(x^2 + y^2)}{r_o^2}\right) \qquad x^2 + y^2 \le r_o^2 \\ h_b(x, y) &= 0 \qquad x^2 + y^2 > r_o^2 \end{aligned} \tag{2.3}$$

and an Ekman pumping of

$$w_e = \alpha(y - L) \qquad y_o < y < L \tag{2.4a}$$

$$w_e = \alpha(y_o - L) = w_{eo} \qquad -y_o < y < y_o \tag{2.4b}$$

$$w_e = -\alpha(L + y) \qquad -L < y < -y \tag{2.4c}$$

(see Fig. 4a). Thus, we work with an isolated parabolic bump of radius r_o; outside of r_o, the bottom is flat. For $\alpha > 0$, this topographic feature is contained wholly within a zone of Ekman pumping, and thus of anticyclonic mean flow tendency. Finally, the Ekman downwelling is uniform over the range $-y_o < y < y_o$. We will always assume $r_o < y_o$, so that the bump occurs in this region.

Assuming R and D are small and that $r_o < x_e$, (2.1b) demonstrates that the lower layer is at rest near the eastern boundary. Eq. (2.1a) in such regions becomes:

$$\beta\psi_{1x} = \frac{f_o w_e}{H_1} \tag{2.5}$$

which in region (2.4a) yields:

$$\psi_1 = \frac{f_o}{\beta H_1}\alpha(y - L)(x - x_e). \tag{2.6}$$

Homogenization theory recognizes that motion in layer 2 can occur only when q_2 develops closed pools. Using (2.6) leads to:

$$q_2 = \beta y + \frac{f_o^3}{g' H_2} \frac{\alpha (y - L)(x - x_e)}{\beta H_1} \tag{2.7}$$

where $\psi_2 = 0$ and we continue to assume $h_b = 0$. A closed zone of q_2 will exist if

$$\frac{\beta g' H_2}{f_o^2} = \frac{f_o}{\beta H_1} \alpha (x_e - x_*) \tag{2.8}$$

for some x_* within the domain. Physically, this implies at x_* the eastward directed Sverdrup flow arrests the westward propagating influence of the eastern boundary. The assumption that x_* exists was assumed by DS and CP, and is equivalent to the idea that the wind-driven flow by itself is sufficiently strong to contact the bottom.

We take the opposite tack, i.e. we assume no x_* between x_w and x_e exists that solves (2.8). Equivalently, the wind-driven flow is too weak to penetrate to the bottom, so that were $h_b = 0$ everywhere, the lower layer in the model would be everywhere at rest. In support of this idea, (2.8) is evaluated using an Ekman pumping value of 10^{-6} m s^{-1}, (yielding $\alpha = 2 \times 10^{-12}$ s^{-1}), $f_o = 10^{-4}$ s^{-1}, $\beta = 2 \times 10^{-11}$ m^{-1} s^{-1}, $H_1 = 10^3$ m, $H_2 = 4 \times 10^3$ m and $g' = .02$ m s^{-2}. Thus $(x_e - x_*) = 16000$ km. Both the Atlantic and the Pacific oceans are thinner than this by a considerable margin.

Thus, everywhere near x_e, $\psi_2 = 0$,

$$\psi_1 = \frac{f_o}{\beta H_1} w_{eo} (x - x_e) \tag{2.9}$$

east of $x = r_o$ (see (2.4b)) and the lower layer potential vorticity resembles that in (2.7). Inside r_o, where the topography is nontrivial, potential vorticity generalizes to

$$q_2 = \beta y + \frac{f_o^3}{g' H_2} \frac{w_e x}{\beta H_1} - \frac{f_o h_{bo}}{H_2 r_o^2} (x^2 + y^2) + \overline{C} \tag{2.10}$$

where $\overline{C}$ is a constant, provided that $\psi_2 = 0$. The previous results guarantee this over at least part of the topography.

Straightforward algebra demonstrates that (2.10) can be written

$$q_2 = \frac{-f_o h_{bo}}{H_2 r_o^2} \left(\left(x - \frac{f_o^2 w_e r_o^2}{2 g' \beta H_1 h_{bo}} \right)^2 + \left(y - \frac{H_2 r_o^2 \beta}{2 f_o h_{bo}} \right)^2 \right) + C \tag{2.11a}$$

where C is a constant. Thus the q_2 contours over the topography correspond to arcs of circles centered on

$$x_c = \left(\frac{f_o^2 w_e r_o^2}{2 g' \beta H_1 h_{bo}}, \frac{H_2 r_o^2 \beta}{2 f_o h_{bo}} \right) \tag{2.11b}$$

which for $h_{bo} > 0$ (as will always be assumed here) is west and north of the center of the topography (see Fig. 4b). Eq. (2.11b) predicts closed potential vorticity contours if $|\mathbf{x}_c| = [x_c^2 + y_c^2]^{1/2} < r_o$, or equivalently, if

$$\frac{H_2 r_o}{2 f_o h_{bo}} \left(\beta^2 + \frac{f_o^6 w_e^2}{g'^2 \beta^2 H_1^2 H_2^2} \right)^{1/2} < 1 \tag{2.12}$$

and hence the possibility of lower-layer flow. The first contribution above indicates if the topography reverses the beta effect in the lower layer (i.e., if $\beta \sim f_o \nabla h_b / H_2$). The second contribution measures the dynamic effect of the wind-driven flow. It is interesting that this contribution always works against the development of closed q_2 contours. The reason may be illustrated for a subtropical gyre by noting that the q_2 values outside of r_o increase when $w_e \neq 0$. The potential vorticity anomaly forced by the topography (which for $h_b > 0$ is a minimum) must therefore be large enough to close in the presence of the larger q_2. In summary, if the resting state q_2 has no closed contours, neither will the forced flow.

On the other hand, using the earlier parameters, the first term is roughly 1000 times larger than the second, thus closed q_2 contours depend largely on the topography. The importance of the static basin structure in determining the flow constitutes a major difference between the present calculations and those of Rhines and Young.

Continuing with the above parameters, (2.12) yields

$$\frac{h_{bo}}{r_o} > 4 \times 10^{-4}. \tag{2.13}$$

Figure 2 suggests $r_o \sim 500$ km, in which case

$$h_{bo} > 200 \text{ m} \tag{2.14}$$

insures that regions isolated from the eastern boundary exist in the open ocean. Recall that both the AP and the ZD are roughly 1000 m in height.

Inside the closed q_2 contours, (2.1b) is area integrated to yield

$$0 = R \oint \nabla q_2 \cdot \mathbf{n} dl - D \oint \nabla \psi_2 \cdot \mathbf{n} dl \tag{2.15}$$

where the line integral is along a constant q_2 contour. Assuming R and D are "small," $q_2 = F(\psi_2)$. Thus (2.15) becomes

$$F' = \frac{D}{R} \tag{2.16}$$

or

$$q_2 = \frac{D}{R} \psi_2 + C_q \tag{2.17}$$

where C_q is a constant.

Eq. (2.17) represents a prediction based on our eddy parameterization which can be tested using eddy-resolving numerical models. Such results will be discussed later; for now we state that (2.17) constitutes a reasonable approximation to our numerical experiments.

The above provides one constraint between ψ_1 and ψ_2, namely

$$\beta y + \frac{f_o^2}{g'H_2}\psi_1 + \frac{f_o}{H_2}h_{bo}\left(1 - \frac{(x^2+y^2)}{r_o^2}\right) = \left(\frac{f_o^2}{g'H_2} + \frac{D}{R}\right)\psi_2 + C_\psi \tag{2.18}$$

where C_ψ is a constant. Upper layer potential vorticity may therefore be evaluated in terms of ψ_1 using (2.18), and (2.1a) thus becomes:

$$J(\psi_1, Q_1) = J\left(\psi_1, \beta y + \frac{f_o^2 \beta y}{g'H_1\left(\frac{f_o^2}{g'H_2} + \frac{D}{R}\right)} + \frac{f_o^3 h_b}{g'H_1H_2\left(\frac{f_o^2}{g'H_2} + \frac{D}{R}\right)}\right) = \frac{f_o w_e}{H_1} + R\nabla^2 q_1 \tag{2.19}$$

which is a linear, nonconstant coefficient equation. Note that Q_1 above differs from q_1, the upper-layer potential vorticity, in that the explicit appearance of the streamfunction has been eliminated. If the last term is neglected, (2.19) corresponds to the modified Sverdrup formula originally derived by DS, although in a context different than the present. As shown in DS, if $H_2 \to \infty$ or $D/R \to \infty$, (2.19) reduces to the reduced gravity result in which all transport is trapped in the upper layer. In less extreme circumstances, ψ_1 is determined by a characteristics integration, where the characteristics Q_1 can be computed ahead of time and ψ_2 is computed from (2.18). DS shows solutions subject to special w_e fields, and CP show that the results of the above integration for planar topography in general lead to interior fronts. The form of (2.19) supports the CP results in general for nonplanar topography.

We here use the special form of our topography to evaluate the characteristics; i.e.

$$\begin{aligned} Q_1 = {} & \frac{-f_o h_{bo}}{H_1 r_o^2\left(1 + \frac{Dg'H_2}{Rf_o^2}\right)} \\ & \cdot \left(x^2 + \left(y - \beta \frac{H_1 r_o^2}{2f_o h_{bo}}\left(1 + \frac{Dg'H_2}{f_o^2}\right)\left(1 + \frac{H_2}{H_1\left(1 + \frac{Dg'H_2}{Rf_o^2}\right)}\right)\right)^2\right) + C_{Q1} \end{aligned} \tag{2.20}$$

where C_{Q1} is a constant. Thus, these characteristics are arcs of circles centered on

$$\bar{\mathbf{x}} = \left(O, \beta \frac{H_1 r_o^2}{2f_o h_{bo}}\left(1 + \frac{Dg'H_2}{f_o^2 R}\right)\left(1 + \frac{H_2}{H_1\left(1 + \frac{D}{R}\frac{g'H_2}{f_o^2}\right)}\right)\right) \tag{2.21}$$

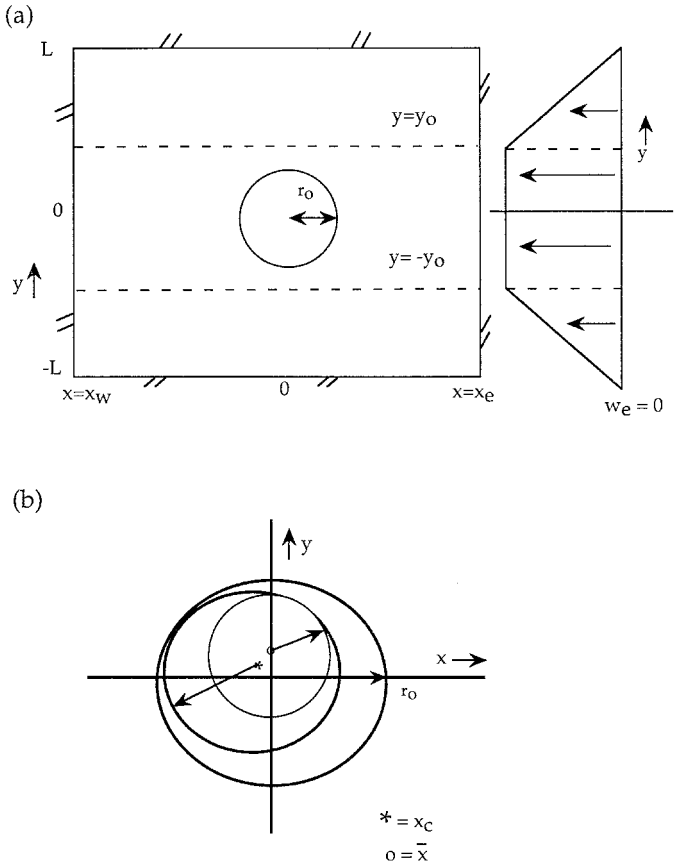

Figure 4. (a) Analytical model topography and Ekman forcing. A radially symmetric parabolic bump is centered in a subtropical gyre. The Ekman pumping field is uniform over the bump, and decreases linearly to zero at the gyre north and south boundaries. The latitudes where the pumping changes are labeled as $\pm y_o$. (b) Critical lower layer contours. The largest circle centered on (0, 0) represents the region of nontrivial topography. The next largest circle, centered on the "*", denotes the largest closed lower layer q_2 contour. The location of the "*" is the point $\mathbf{x}_c$ defined by (2.11). The smallest circle, centered on the 0, denotes the largest closed Q_1 contour. This circle is centered on $\overline{\mathbf{x}}$, defined by (2.21).

and we expect the results of the method of characteristics solution proposed by DS and CP to apply on all open Q_1 contours. On the other hand, if $\overline{\mathbf{x}}$ is within the region of closed q_2, some Q_1 characteristics will be closed (see Fig. 4b). The characteristics methodology must then fail in such zones, for the simple reason that w_e is one signed everywhere on the trajectory. Rather, an area integral over a closed Q_1 region demonstrates that eddy effects (i.e. potential vorticity diffusion) are required to achieve a balance, i.e.

$$O = \frac{f_o}{H_1} \iint w_e \, dA + R \oint \nabla q_1 \cdot \mathbf{n} dl. \tag{2.22}$$

The physics in (2.22) are that the Ekman pumping, w_e, introduces mass into the upper layer, the removal of which thus must occur by eddy processes. Our eddy parameterization is essentially that of down-gradient thickness diffusion (see 2.1b), hence the balance in (2.22). This balance essentially generalizes the original Welander (1968) barotropic result and is a main point of this paper.

The relevance of (2.22) depends upon the simultaneous existence of closed q_2 and closed Q_1 regions. It is thus important to ask if the parametric regime in which this occurs pertains to the ocean.

The radius of the largest full q_2 circle is $r_o - |\mathbf{x}_c|$, where $\mathbf{x}_c$ is given by (2.11b). The existence of closed Q_1 thus requires:

$$r_o - |\mathbf{x}_c| > |\overline{\mathbf{x}} - \mathbf{x}_c|. \tag{2.23}$$

It turns out for the parameters under consideration that (2.23) can be met if closed q_2 contours exists. First, recall that the meridional displacement in (2.11b) is orders of magnitude greater than the zonal displacement; thus, $|\mathbf{x}_c| \cong |y_c|$ and (2.23) becomes

$$r_o > \overline{y}. \tag{2.24}$$

The evaluation of $\overline{y}$ depends both upon h_{bo} and the ratio $X = Dg'H_2/f_0^2R$. For the former we choose $h_{bo} = 1000$ m (see Fig. 1); the latter is difficult to estimate since neither D nor R are well known. Acknowledging this uncertainty, a typical Ekman layer thickness is 0 (10 m). Eq. (2.2) then suggests:

$$X = \frac{Dg'H_2}{f_0^2R} \cong \frac{R_o}{R} \tag{2.25}$$

where $R_o = Dg'H_2/f_0^2$. If $D = 1/40$ days, $g' = .02$ cm s^{-2}, $H_2 = 4000$ m and $f_o = 10^{-4}$ s^{-1}, $R_o = 2000$ m^2 s^{-1}.

First, for small X (i.e. $R > 2000$ m^2 s^{-1}), $\overline{y}$ is independent of X at leading order and becomes

$$\overline{y} = \frac{\beta r_0^2(H_1 + H_2)}{2f_0h_{bo}} = \frac{\beta r_0^2 H}{2f_0h_{bo}} \tag{2.26}$$

which leads to the criterion for closed $f/(H - h_b)$ contours in a barotropic fluid. The ratio of the meridional displacements (2.26) and (2.11b) is $\overline{y}/y_c = (1 + H_1/H_2)$, and since $H_1/H_2 \simeq .25 < 1$ for the wind-driven circulation, the satisfaction of (2.12) often implies for small X that (2.23) is met.

Support for the downgradient thickness diffusion parameterization (essentially like our downgradient q diffusion) has been recently provided by Danabasaglu et al. (1994), who found their noneddy resolving climate model results were improved using an $R \sim 0$

(10^3 m^2 s^{-1}). We therefore also evaluate (2.24) for the cases $X = 2$ and 4, corresponding, for example, to a 10 m Ekman depth (spin down time of 40 days) and a q diffusion of either $.5 \times 10^3$ or 10^3 m^2 s^{-1}. In these cases (2.24) yields:

$$\frac{\bar{y}}{r_o} = .44, \qquad .56 < 1$$

and closed Q_1 contours are still formed.

Finally, the critical X beyond which (2.24) cannot be met requires $\bar{y}/r_o = 1$, and yields $X = 9$. Assuming $R = 10^3$ m^2 s^{-1}, this implies a bottom friction spin down time of 10 days, or a vertical viscosity of .3 m^2 s^{-1}. Weatherly (1984) has estimated the net energy dissipation under the Gulf Stream Current water from observations. Converting his drag coefficient into an eddy viscosity yields $A_v = .16 \times 10^{-2}$ m^2 s^{-1}, where a bottom velocity scale of 10 cm s^{-1} and bottom boundary layer thickness of 10 m has been assumed. Thus our critical vertical viscosity is larger than values obtained from the literature, suggesting the simultaneous existence of closed barotropic potential vorticity $f/(H - h_b)$ contours and Q_1 contours. This implies for topography like the ZD and the AP that the stratified general circulation can be put into the paradoxical situation that surface circulation is directly influenced by the bottom Ekman layer.

Computing ψ_1 inside closed Q_1 by (2.22) requires the solution of a second order equation. This can be obtained analytically for the present, simple geometry. Centering the coordinate system on $\bar{x}$, Q_1 depends only on the radial coordinate, ρ. Since w_e is uniform (see 2.4b), (2.22) becomes:

$$q_{1\rho} = \frac{-f_o w_e \rho}{2H_1 R} \tag{2.27}$$

hence

$$q_1 = \frac{-f_o w_e \rho^2}{4H_1 R} + C_{q1} \tag{2.28}$$

where C_{q1} is a constant.

The definition of q_1, (2.7), and the solution for q_2, (2.11), now represent two equations for the two unknowns ψ_1 and ψ_2. The quantity ψ_1, is:

$$\psi_1 = \frac{w_e \rho^2 f_o}{4DH_2}(1 + X) + \frac{h_{bo} f_o R}{DH_2}\left(1 - \frac{\left(x^2 + \left(y - \frac{\beta g' H_1 r_o^2}{2f_o^2}\left(1 + \frac{H}{H_1 X}\right)\frac{DH_2}{f_o h_{bo} R}\right)^2\right)}{r_o^2}\right) + C_{\psi 1} \tag{2.29}$$

and thus

$$\psi_2 = \frac{w_e \rho^2 f_o}{4DH_2} + \frac{h_{bo} f_o R}{DH_2}\left(1 - \frac{\left(x^2 + \left(y - \frac{\beta H r_o^2}{2 f_o h_{bo}}\right)^2\right)}{r_o^2}\right) + C_{\psi 2}. \tag{2.30}$$

The above two formulae, along with their implied total transport $T = H_1\psi_1 + H_2\psi_2$, emphasize that inside zones topographically shielded from the eastern boundary, the flow and total transport are controlled by bottom friction. This is demonstrated by the appearance of D in the denominator of (2.29) and (2.30). Note also in the weak bottom friction limit (i.e. small X), the geostrophic contours are effectively given by the barotropic $f/(H - h_b)$ contours, and

$$\psi_1 = \left(\frac{w_e f_o}{4DH_2} - \frac{h_{bo} f_o R}{DH_2 r_o^2}\right)\left(x^2 + \left(y - \frac{\beta H r_o^2}{2 f_o h_{bo}}\right)^2\right) + C_{\psi 1} \tag{2.31}$$

$$\psi_2 = \psi_1\left(1 + O\left(\frac{D}{R}\frac{g' H_2}{f_o^2}\right)\right) \tag{2.32}$$

$$T = (H_1 + H_2)\psi_1\left(1 + O\left(\frac{D}{R}\frac{g' H_2}{f_o^2}\right)\right). \tag{2.33}$$

The inverse dependence on bottom friction is evident, but it is also the case that the flow is barotropic at leading order (see 2.32).

An evaluation of (1.5) demonstrates that the first term in (2.31) corresponds to the Welander (1968) result. The second term is thus unambiguously identified as the effect resulting from the generalization of Welander's work to include stratification. It is curious that the g' stratification parameter makes no explicit appearance here. Rather, the stratification appears implicitly in the R parameter. It is also interesting that the ratio of the effects is:

$$\frac{w_e r_o^2}{4Rh_b} = \frac{10^{-6}\ \mathrm{m^2\ s^{-1}}\ (5 \times 10^5\ \mathrm{m})^2}{4\ 10^3\ \mathrm{m^2\ s^{-1}}\ 10^3\ \mathrm{m}} = .06 \ll 1 \tag{2.34}$$

using typical numbers, and suggests that the eddy driving is an important contributor.

Larger and more realistic bottom frictions (larger X) decrease the amplitude of the bottom flow and the area enclosed within the critical Q_1 contours, but nonetheless directly determine the transport. This should be contrasted with the case where closed geostrophic contours occur for reasons other than the topographic amplitude, and hence the existence of lower layer regions isolated from the eastern boundary is independent of D.

The reason for the sensitivity to D in (2.29), (2.30) is related to the physics occurring in the purely barotropic problem. There, the bottom Ekman layer was solely responsible for

balancing the mass budget by exporting fluid at the same rate as it was supplied by the surface Ekman layer. In the stratified problem, down-gradient potential diffusion acts effectively like a thickness flux; therefore for closed Q_1 contours, the uppermost layer balance is achieved through R (see Fig. 3, which illustrates the weak bottom friction limit of the three-layer model described in the Appendix). This balance determines the interface separating the layers. The deeper layer, however, also reacts to mean potential vorticity anomalies and tries to diffuse them away. This in turn accelerates the deepest layer, where bottom friction is active. In the limiting case of weak bottom friction, part of the bottom Ekman layer mass flux balances the mass input from the surface Ekman layer.

3. Numerical experiments

The previous section has described purely analytical calculations employing an approximate form of the quasi-geostrophic equations and an eddy parameterization. The question remains as to whether such solutions are realized in more complete models in which, for example, the eddies are explicit, rather than parameterized. We here test this using a standard, well-known quasi-geostrophic model (see Holland, 1978). We have chosen three rather than two layers because we have found that the former generates a more vigorous eddy field than the latter.

The average layer thicknesses are 300 m, 700 m and 4000 m, and the reduced gravities are .014 m s^{-2} and .007 m s^{-2}, which yield deformation radii of 29 and 16 km. A 10 km grid resolution was used in a rectangular 301 $\times$ 201 configuration. Biharmonic viscosity was employed with a coefficient of $-1 \times 10^{+10}$ m^4 s^{-1}. A single subtropical gyre was modeled and the Ekman pumping field decreased linearly from a value of zero at the north and south model boundaries to a minimum value of -1×10^{-6} m s^{-1} in the middle of the basin. These model parameters were fixed for all the experiments shown here. The remaining two parameters, bottom friction and topographic amplitude, were varied. Bottom friction ranged from values of 5×10^{-8} s^{-1} to 5×10^{-9} s^{-1}, corresponding to spin-down times from 200 days to 2000 days. These bottom drags are weaker than those which have been used in the past (Kawase, 1993; Thompson, 1995). We will have more to say about this in a moment.

The bottom topography employed in these experiments consists of a nonsymmetric Gaussian bump. This was done because the Gaussian is smooth, whereas models with a parabolic bottom shape generated grid-scale noise at the discontinuity in the first derivative. The amplitude of the bump was varied between 300 m and 1000 m. (Note that the amplitude of the AP and the ZD are both roughly 1200 m.) The e-folding scales of the bump were 350 km zonally and 450 km meridionally. A plot of the model topography appears in Figure 5a along with a plot of $q_3 = \beta y - (f_0 h_b / H_3)$ in Figure 5b. The latter is the ambient potential vorticity field of the abyssal layer.

The topographic anomaly was placed in the southwestern quadrant of the gyre where, according to analytical calculation, q mixing drives a mean flow in layer 2. The model also

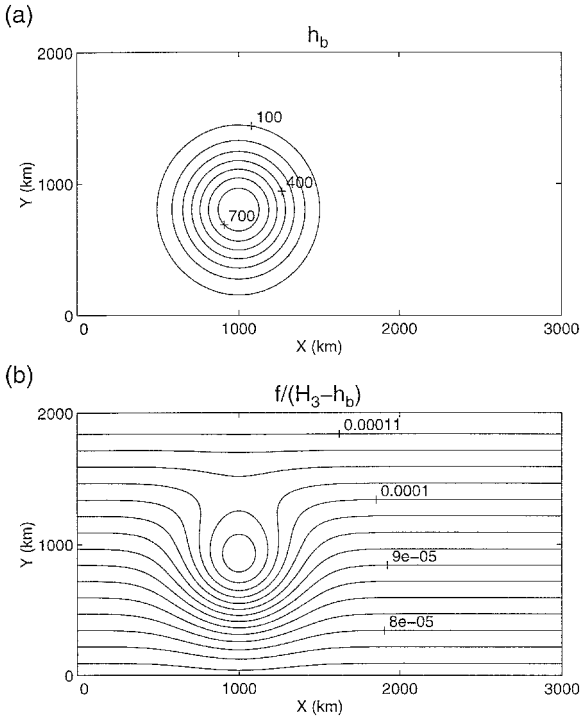

Figure 5. Numerical model topography. A Gaussian bump with e-folding scales of 350 km and 450 km in the zonal and meridional directions respectively appears in (a). The position is roughly under the analytically expected second layer uniform q_2 pool and south of the inertial third layer recirculation. The topography height is 800 m, CI = 100 m. In (b) is the potential vorticity the third layer would have in the absence of motion. Note the region of closed q_3 over the topography. CI = 2.5×10^{-6} s^{-1}.

generates a vigorous eddy-driven inertial recirculation, but the topography in Figure 5a is south of it. Thus, circulations developed over the topography will reflect eddy-form drag forcing of the lower layer by the upper layer, rather than a response to a mean flow in the lowest layer. The latter problem has been studied extensively by Rhines (1989).

However, the AP exists between the two relatively deep extension currents of the Gulf Stream, i.e. the North Atlantic Current and the Azores Current (Sy, 1988). Similarly, the Zapiola Drift occurs south of the Malvinas-Brazil Current Confluence and eastward extension. Thus the environment near both our example topographies is dynamically complex, and only part of that is captured in our numerical experiments.

We show in Figure 6 the three-layer average streamfunctions from a flat bottom experiment. These were obtained by averaging over the last 10 years of a 30-year run. The bottom friction coefficient here was 5×10^{-9} s^{-1}. The most notable features are the intense inertial recirculations found in the north quarter of each layer. Aside from this, the upper layer is dominated by the large-scale anticyclonic flow which fills the entire basin and joins

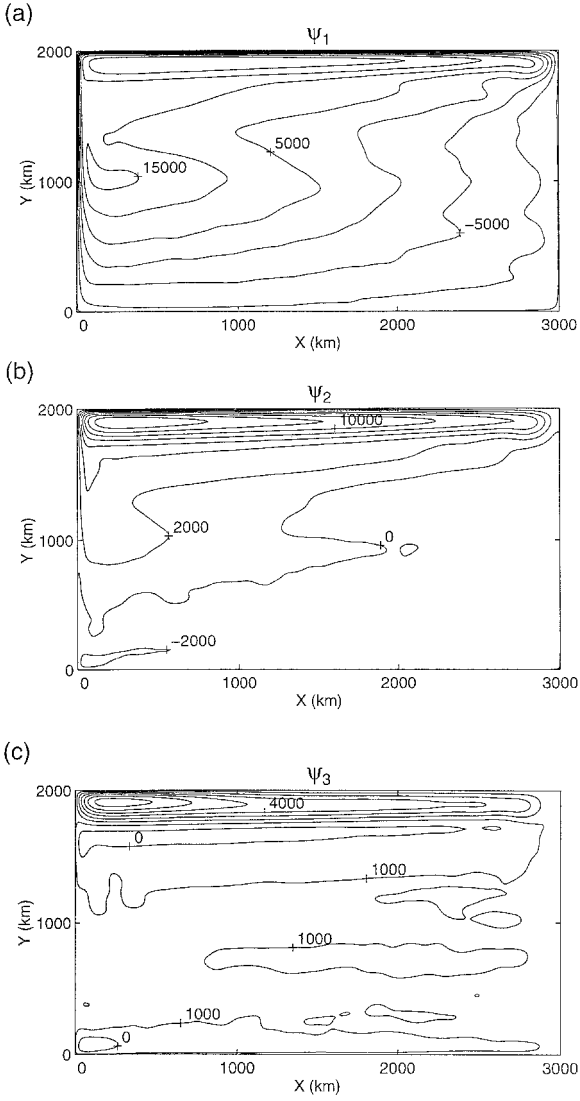

Figure 6. Flat bottom results. The average velocity streamfunction for the (a) first, (b) second and (c) third layers are shown. CI = 5000 m^2 s^{-1} in (a), 2000 m^2 s^{-1} in (b) and 1000 m^2 s^{-1} in (c). These were obtained from averaging the last 10 years of a 30-year run. Parameters come from the standard set and bottom drag $D = 5 \times 10^{-9}$ s^{-1}.

with a western boundary current. The second layer, away from the inertial recirculation, also possesses an anticyclonic circulation. Roughly speaking, the region in which the second layer is in motion is in agreement with the predictions of homogenization theory. Finally, the third layer is essentially at rest aside from the inertial recirculation, again in keeping with theoretical expectations.

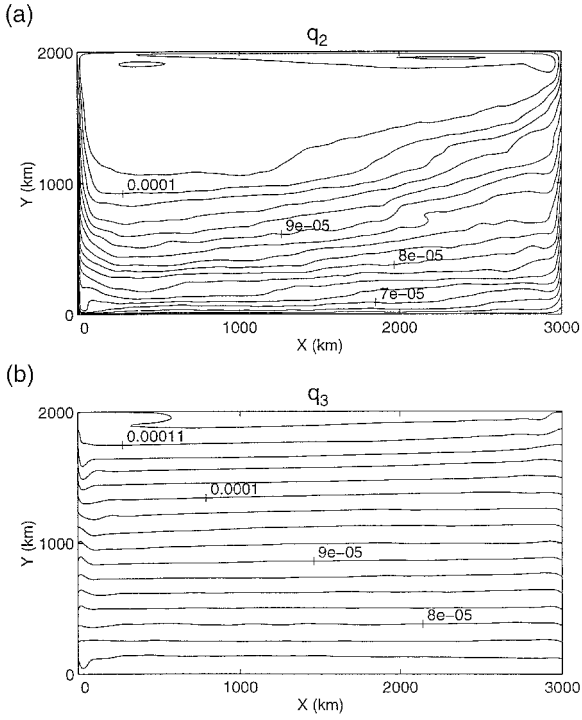

Figure 7. (a) Second and (b) third layer 10 year averaged potential vorticities for the experiment in Figure 6. CI = 2.5×10^{-6} s $^{-1}$.

The second and third layer 10-year averaged potential vorticities from this same run appear in Figure 7. A region of decreased q_2 gradients in the second layer coincides with the moving region in Figure 7b. The third layer potential vorticity field is dominated by planetary vorticity, as expected. Overall, the numerical mean results are a reasonable facsimile of the analytically predicted fields.

The results of an experiment with the same parameter settings as above, but with a Gaussian topography of 800 m height in the third layer appear next. The last 10 years of a 40-year run were averaged to yield mean layer streamfunctions for all layers (Fig. 8) and layers 2 and 3 potential vorticities (Fig. 9). The most noticeable feature of these results occurs in the third layer maps, where a 60 Sv anticyclonic circulation, centered over the topography, appears in the third layer. Similar features are found in the upper layers. Further, the potential vorticity field associated with this feature is reduced in amplitude from that of the resting field seen in Figure 5b.

a. Eddy parameterization

Our analytical model parameterized eddies using a down-gradient potential vorticity diffusion and this allowed a rather complete characterization of the flow. Here, we examine this parameterization.

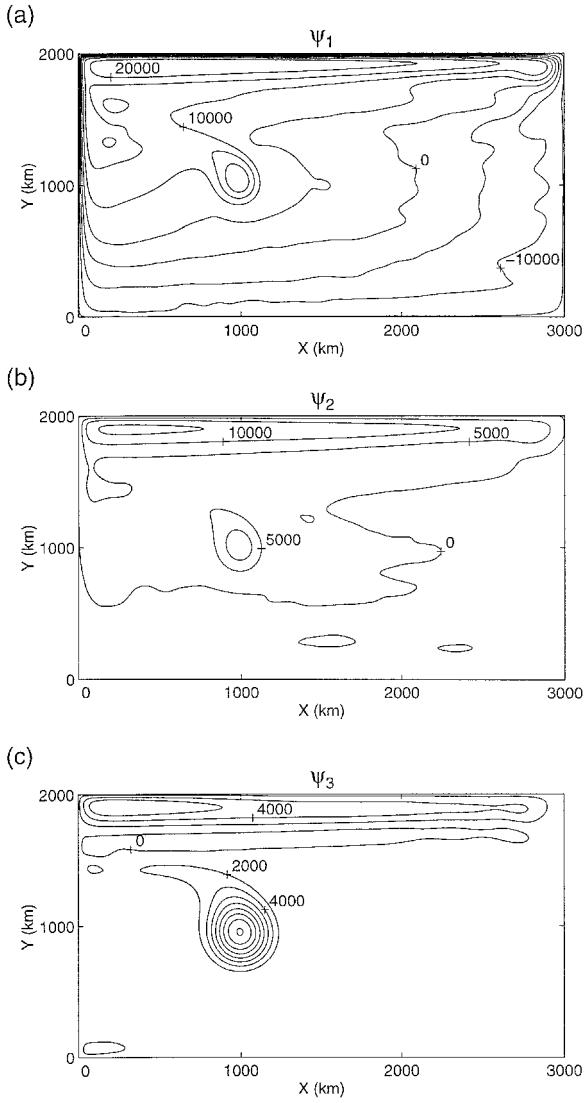

Figure 8. Plot as in Figure 6, except with an 800 m bottom bump. The bump location appears in Figure 5a. Bottom drag $D = 5 \times 10^{-9}\,s^{-1}$. CI = $5000\,m^2\,s^{-1}$ in (a), $5000\,m^2\,s^{-1}$ in (b), $2000\,m^2\,s^{-1}$ in (c). Note the strong anticyclone centered on the topography in layer 3, and appearing in layers 1 and 2. The bottom layer transport is 60 Sv and the total transport over the bump is roughly 72 Sv.

The most important prediction of this parameterization is (2.17), which linearly relates abyssal potential vorticity to abyssal streamfunction with a coefficient directly dependent on bottom friction. This relation influences the later formulae for surface streamfunction and net transport and thus has a quantitative impact on the analytical results.

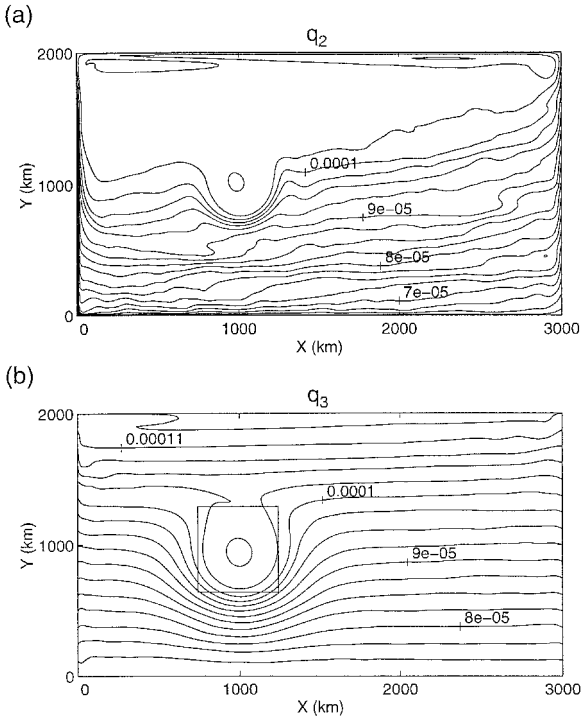

Figure 9. Plot as in Figure 7, but for the experiment shown in Figure 8. CI = 2.5×10^{-6} s^{-1}. Note the alteration in q_3 relative to Figure 5b. The box encloses the area discussed in Figure 10b.

A scatter plot of q_3 versus ψ_3 for the experiment described above appears in Figure 10a. The majority of the points are clustered around a small constant ψ_3, as expected for a layer largely at rest in the mean. The two exceptions to this occur for large q_3 (i.e. in the model inertial recirculation) and for moderate q_3, where the streamfunction values increase to roughly 16000 m^2 s^{-1}. The latter is clearly associated with the topography and is consistent with a linear ψ_3, q_3 relationship.

Figure 10b compares $q_3 - \psi_3$ scatter plots from three different experiments. Here the points come from the area of the topographic anomaly shown by the inset box in Figure 9. The three experiments used differing bottom drags, i.e. $D = 5 \times 10^{-8}$ s^{-1}, 1×10^{-8} s^{-1} and 5×10^{-9} s^{-1} (see the labels).

Note that increasing D is associated with increasing slope, consistent with the predictions of (2.17). There is also quantitative consistency with this relationship. Least squares linear fits to the $q_3 - \psi_3$ data appear in Figure 10b as the light solid lines. Note, a subset of the data has been used for the fit, consistent with the idea that some of the data pairs in Figure 10b come from outside the shielded area, and thus should not be described by (2.17). The fitted slopes are, in order of decreasing D, 3.7×10^{-9} m^{-2}, 2.9×10^{-10} m^{-2}

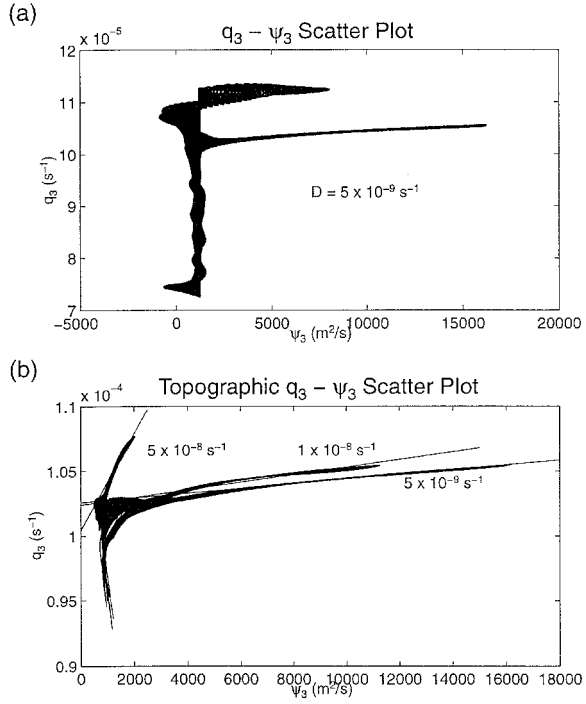

Figure 10. (a) $q_3 - \psi_3$ relationship for the experiment in Figure 8. Results for the entire basin are displayed. The branch occurring at mid q_3 value comes from the boxed area around the topography in Figure 9. This branch of the $q_3 - \psi_3$ plot appears again in (b), along with $q_3 - \psi_3$ plots from two other experiments. These experiments are differentiated by their values of D, which are used to label the plots. Note the decrease in the slope as D decreases, consistent with the predictions based on down-gradient q_3 mixing. The light solid lines are the result of a least squares linear fit to the scatter plot.

and 1.8×10^{-10} m^{-2}. The ratio from greatest to least is 20, in keeping with the factor of 10 change in D. The slope ratio for the two weakest D experiments is 1.6, close to the factor of 2 difference in the associated D's. While the respective slope ratios are not exactly those of the associated D's, the order of magnitude variation is clearly reproduced. Also, an unknown parameter in the comparison is R, the eddy potential vorticity mixing coefficient. It is likely that this parameter does exhibit some dependency on D. In total, the above results support the assertion that the eddy parameterization (2.17) does not qualitatively damage the analysis.

Finally, the slope estimates allow for an estimation of R. The average value for the three experiments in Figure 10b is R = 24 m^2 s^{-1}, which is quite small relative to the 10^3 m^2 s^{-1} estimate mentioned in the preceding section. These apparently low R values constitute the reason for our choice of unusually weak D values; namely, we were interested in numerically exploring the parameter regime $X \simeq 0(1)$, where $X = Dg''H_3/f_0^2R$. Using the R

values diagnosed for each experiment and our other parameters, we obtain X values of 9, .9 and .5 in order of decreasing D.

It is possible that the weak R values reflect the numerical configuration of our experiment; a different setup could generate more vigorous eddy mixing, which in turn should yield results like those shown when employing larger bottom drags. A separate interpretation of our experiments is that larger drags, more in line with classical values, generate much weaker trapped circulations.

Based on the above X estimates, the latter two experiments should fall into the category where the layer 1 balance is described by the three-layer equivalent of (2.22). Note the ψ_1 and q_1 structure appearing in Figures 8a and 9a, where closed contours are found. This is in agreement with our analytical expectations, and should be contrasted with the results appearing in Figure 11, which exhibits ψ_1 from the experiment with $D = 5 \times 10^{-8}$ s $^{-1}$ ($X = 9$). Here we don't anticipate the successful penetration of the deep flow to the surface, and thus that ψ_1 will resemble the flat bottom results in Figure 6. This is clearly the case for Figure 11, in spite of a nontrivial 6 Sv anticyclonic transport in layer 3.

There are at least three other qualitative predictions from the analytical theory which merit numerical examination. First, third layer and total transport should vary directly with h_{bo} once closed $f/(H - h_b)$ contours are established. Second, third layer and total transport should be inversely proportional to bottom friction. These two dependencies are suggested by (2.33). Last, the sense of the net transport should be independent of the sign of the Ekman pumping. This is suggested by (2.34) which argues T is dominated by the topography.

We have performed experiments to examine these points. The first is illustrated in Figure 12, where the maximum average streamfunction amplitude in the abyssal layer over the topographic anomaly is plotted against the amplitude of the topography. All other parameters were held constant and $D = 5 \times 10^{-9}$ s^{-1}. Note the increase in streamfunction amplitude with increasing h_{bo}, as expected.

The dependence on D appears in Figure 13, where the abyssal streamfunction maximum amplitude is plotted against bottom friction. In all these experiments, a Gaussian bottom anomaly of 800 m was used. Note the dramatic increase in ψ_3 which occurs for $D < 2 \times 10^{-8}$ s^{-1}. For D greater than this, transport is weakly sensitive to bottom friction. The overall structure is consistent with an inverse dependence of transport on D, again as expected.

Finally, in Figure 14, we plot the three streamfunction fields from an experiment with a cyclonic Ekman pumping. The parameters are standard, $D = 5 \times 10^{-9}$ s^{-1} and $h_{bo} = 1000$ m. The upper layer streamfunction appearing in Figure 14a shows the expected cyclonic circulation pattern of a subpolar gyre. Nonetheless, appearing in the second and third layers are sizable anticyclonic circulations. The total transport is 53 Sv between them, with 50 Sv appearing in layer 3. This supports the theory, which predicts the anomalous transport depends largely on the sign of the topographic anomaly.

Thus, the analytical theory and numerical experiments are in qualitative and quantitative

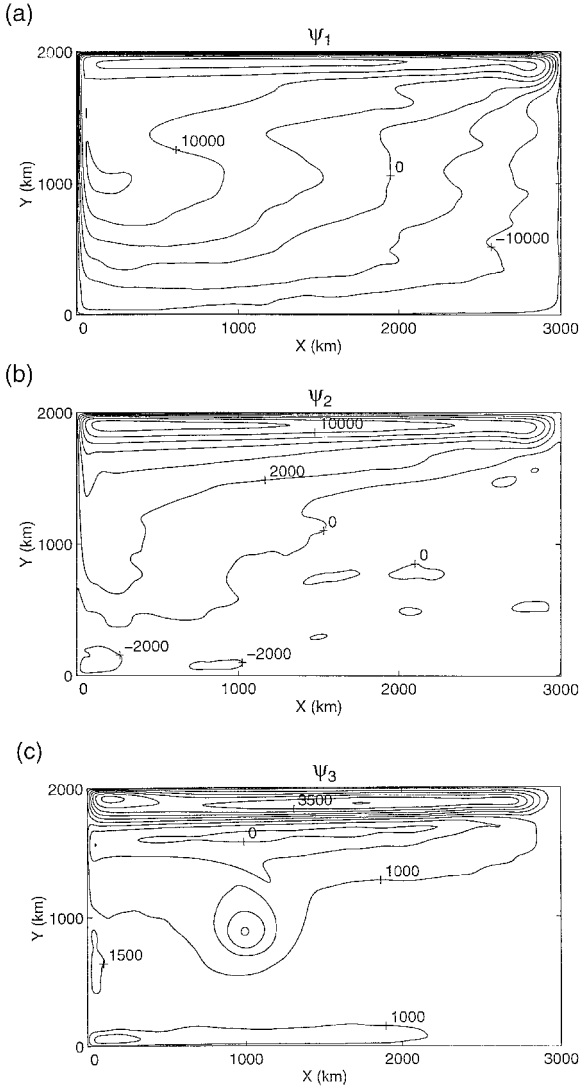

Figure 11. Strong bottom drag results. Plot as in Figure 6, but with 800 m topography and $D = 5 \times 10^{-8}\ s^{-1}$. CI = 5000 $m^2\ s^{-1}$ in (a), 2000 $m^2\ s^{-1}$ in (b) and 500 $m^2\ s^{-1}$ in (c). Note the reduced ψ_3 amplitude here relative to Figure 8. The lower-layer transport around the bump is roughly 6 Sv.

agreement. Eddies appear to be capable of accelerating the deep flow around topographically closed geostrophic contours, which in turn is an effect reasonably parameterized by a down-gradient potential vorticity diffusion. For topography of amplitudes like those found in the North and South Atlantic, barotropically closed contours also appear. This involves an interesting interplay between eddies and forcing. The upper layer is, of course, directly forced. The lower layers, however, are accelerated by the eddies generated ultimately by

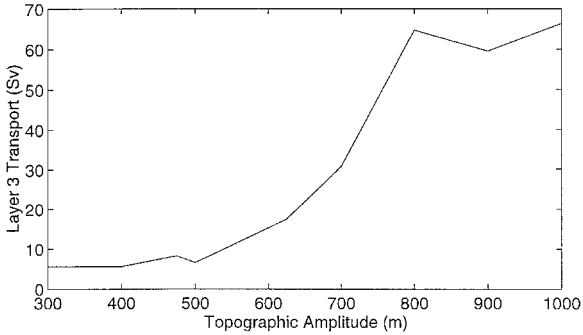

Figure 12. Maximum third layer streamfunction versus topographic amplitude. The ψ_3 values were selected from the area of the topography. Parameters are standard and $D = 5 \times 10^{-9}\ s^{-1}$. The net transport varies directly with h_{bo}, as predicted by the theory.

the wind-driven flow instability and the abyssal flow amplitude is ultimately arrested by bottom friction. It is interesting that the latter can kinematically dominate the mean flow, and modify the dynamics of the surface flow.

4. Discussion

The theory in this paper argues that localized topographic anomalies like those found in the North and South Atlantic can play a major role in determining regional circulation characteristics. The related effects are two fold. Perhaps most importantly, localized topography generates topographically closed geostrophic contours, which then represent areas where the wind-driven flow can easily penetrate to the bottom. This is in contrast to the dynamically closed geostrophic contours which occur in homogenization theory. Wind-driven flow appears to be too weak to penetrate to the ocean floor via this mechanism.

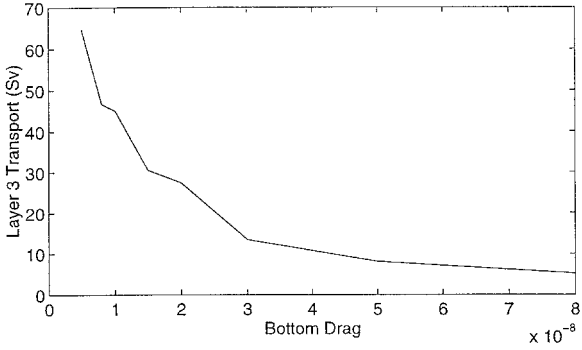

Figure 13. Maximum third layer streamfunction versus bottom drag. The parameters are standard and $h_{bo} = 800$ m. The transport varies inversely with D, as predicted by the theory.

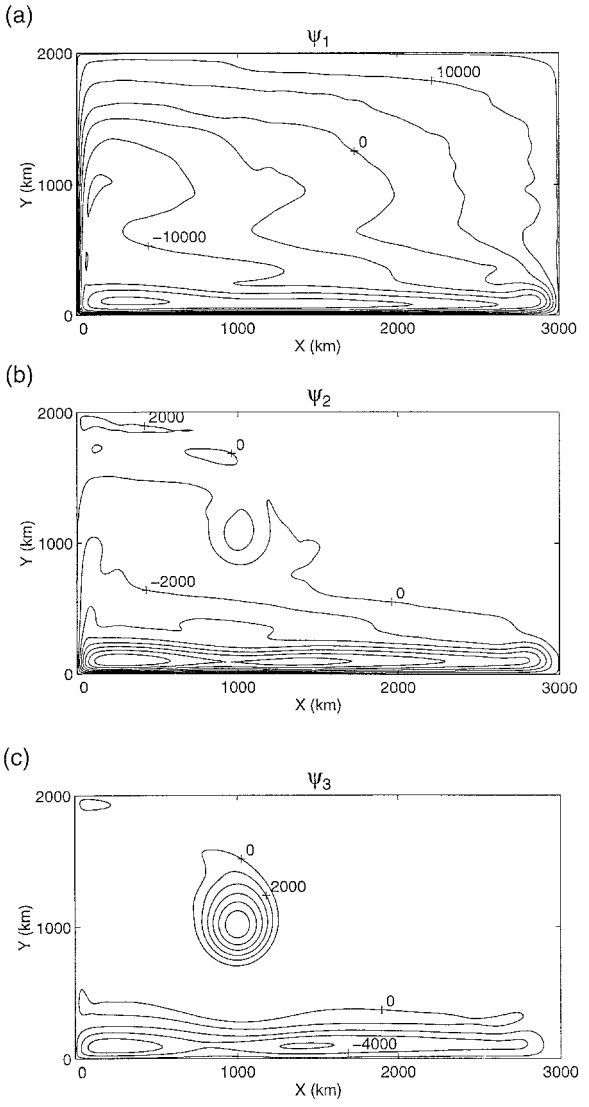

Figure 14. As in Figure 6, but with 1000 m topography and cyclonic Ekman suction. CI = 5000 $m^2\ s^{-1}$ in (a), 2000 $m^2\ s^{-1}$ in (b) and 2000 $m^2\ s^{-1}$ in (c). A subpolar gyre dominates the surface flow, while the flow around the bump is anticyclonic, in agreement with the theory. The layer 3 transport is roughly 50 Sv.

The second effect is that, depending upon the sizes of bottom friction and topographic amplitude, barotropic closed geostrophic contours, effectively a generalization of $f/(H - h_b)$, can appear. Purely barotropic general circulation models with topography generate areas isolated from the eastern boundary. Our results here show a similar result is obtained in a

stratified fluid. Further, our scaling arguments suggest that the onset of barotropically closed contours and topographically closed geostrophic contours for the abyssal layers can be nearly coincident. If the entire water column is shielded, the flow regime throughout the water column is controlled by bottom friction, and to a large extent, transport is inversely proportional to bottom friction.

In a broad sense then, the existence of closed $f/(H - h_b)$ contours is a strong indicator that the dynamics presented in this paper are relevant to that area. To this end it is interesting that both the AP and the ZD meet this criterion (see Fig. 2). We are thus motivated to consider the application of the present results to those two regions.

Perhaps the feature that is apparently most clearly shared by the two areas is that the mean flows over the topographic anomalies, should they exist, are characterized by anticyclonic (poleward on the west, equatorward on the east) transport. The evidence supporting this for the AP includes several sources, most notably Sy (1988), Klein and Seidler (1989) and Pollard *et al.* (1996). The Zapiola Anticyclone is apparent in Saunders and King (1995a,b) and corroborating long-term current meter measurements are provided by Weatherly (1993). Given that both topographic anomalies are highs, the present theory provides an explanation for the sense of the flow. Also, the apparent tendency for the AP transport estimates to increase with increasing depth (compare Klein and Seidler with Sy) suggests the relevance of the theory.

However, a distinction between the AP and ZD lies in their transport; the Zapiola Anticyclone carries in excess of 100 Sv and the AP flow no more than 15 Sv. A second important distinction lies in the nature of the surface flow. Clearly, the AP is found entirely within the NA subtropical gyre (see Fig. 2), while the ZD is found south of the Brazil Current-Malvinas Current, implying the ZD topography is outside the South Atlantic subtropical gyre. A theory which claims to describe general circulation dynamics over closed geostrophic contours must therefore also be able to explain how two such very different anticyclones can arise. It is interesting, if perhaps fortuitous, that the present theory provides such explanations. We begin with the latter point.

The analytical calculations for total transport, appearing in (2.33), along with the estimate in (2.34), demonstrate the insensitivity of the circulation to the large-scale features of the surface circulation. Numerical support of this point appears in Figure 14. Rather, it is the sign of the topographic anomaly that determines the flow and this is common to the AP and the ZD.

The much more dramatic kinematic distinction between these areas, however, also can be accounted for, even if the explanation to follow is qualitative. The explanation is based on the distinctions in the bottom conditions, and these appear in Figures 1 and 2. For example, it is clear that the AP is a feature of the Mid-Atlantic Ridge, and the associated topography there is complex and variable on a broad spectrum of spatial scales. In contrast, the ZD is a depositional feature and the bottom is routinely referred to as a mud wave plain. In contrast to the MAR topographic variability, mudwaves of 10's of m are a dominant

feature. Indeed, models of their development have been a focus of past studies (Flood and Shor, 1988; Blumsack and Weatherly, 1989; Weatherly, 1993). The important comparative point here is that relatively speaking, the ZD is a very smooth bottom feature compared to the AP. This implicitly appears in Figure 2, where Figure 2a is a contour plot of smoothed data (3 passes with a 9 point equal weight filter), while Figure 2b is a plot based on raw bottom data. A comparison of the bottom data, once smoothed, for both regions is available in Figure 1.

For the purposes of the present model, this translates into a considerable difference in bottom drag. It is unclear at the present how to quantitatively relate these very different bottom types to D, but it seems reasonable to associate larger D's with the AP rather than the ZD. The existence of closed geostrophic contours for both regions makes them prime candidates for bottom friction control as described in the present paper, so the existence of a greater transport over the ZD than the AP is in line with the different bottom topographies.

We have demonstrated in this paper that net transports of 0 (100 Sv) over topography are possible for weak bottom friction (see Fig. 8). Thus we might argue that the ZD is characterized by $X \cong (.1 - .2)$. Recall also that full penetration of the deep flow to the surface-generated closed potential vorticity regions in the near-surface flow. This implies the mean circulation will have the same sense as the deep flow. There is no clear indication of anticyclonic flow in the near surface from the WOCE A-11 cruise. On the other hand, the 200 m ADCP data in Saunders and King (1995) provide an instantaneous glimpse of the near-surface flow, so the lack of a clear signal does not necessarily represent a failure of the theory.

Increasing the bottom drag by an order of magnitude results in our numerical experiments in a reduction of net transport to roughly 0 (10 Sv). This is not unlike the values proposed for the AP by Pollard *et al.* (1996) and Sy (1988). The weak near-surface circulations proposed by Klein and Seidler (1986) of 1.5 Sv relative to 800 m, and their tendency to wax and wane with the seasons also hint that the circulation is more pronounced at depth. This also is consistent with the structure of the solutions proposed here.

In summary, we suggest the ZD and AP are examples of eddy-driven flow over topography where the transport amplitude is sensitive to bottom drag. The large ZD anticyclone reflects weak drag while the AP, on the other hand, is much more strongly damped. The dynamical balance is distinct from the classical Sverdrup paradigm.

We have focused here on the Atlantic. A quick examination of the Pacific reveals a scarcity of large-scale closed $f/(H - h_b)$ regions, although smaller scale areas exist. The Indian Ocean is a somewhat richer environment and it would be interesting to visit relevant observations given these calculations. Also, better bottom boundary layer models than the simple one used here are available, and would help to address the relative importance of the AP and ZD bottom types to transport in a more quantitative way.

Acknowledgments. Conversations with Bernard Barnier, Yves Desaubies, Rui Xin Huang and Georges Weatherly were very useful. This project was started while WKD was a visitor at the Institut de Mecanique de Grenoble, and the hospitality of the scientists of that institution is gratefully acknowledged. The quasi-geostrophic calculations were supported by an internal grant from the Academic Computing and Networking Services of the Florida State University. Ms. Jane Jimeian assisted with the computational tasks and Ms. Sheila Heseltine prepared the figures and the text. WKD is supported by NSF grants OCE-9401977 and OCE-9617728 and NASA grant NAGW-4883.

APPENDIX

A three-layer example

It is interesting to consider the results of Section 2 to three layers for the reasons that the shallow oceanic wind-driven flow exists in a stratified fluid itself partly set into motion by Rhines and Young mechanics. A three-layer model thus allows for interaction between subsurface layers of uniform potential vorticity and topographically closed bottom layer geostrophic contours. Further, this solution is useful for comparison with the numerical investigations in Section 3.

The three-layer equations are:

$$J(\psi_1, q_1) = \frac{f_o w_e}{H_1} + R\nabla^2 q_1, \qquad q_1 = \beta y + \frac{f_o^2}{g' H_1}(\psi_2 - \psi_1) \tag{A.1}$$

$$J(\psi_2, q_2) = R\nabla^2 q_2, \qquad q_2 = \beta y + \frac{f_o^2}{g' H_2}(\psi_1 - \psi_2) + \frac{f_o^2}{g'' H_2}(\psi_3 - \psi_2) \tag{A.2}$$

$$J(\psi_3, q_3) = R\nabla^2 q_3 - D\nabla^2 \psi_3, \qquad q_3 = \beta y + \frac{f_o^2}{g'' H_3}(\psi_2 - \psi_3) + \frac{f_o h_b}{H_3} \tag{A.3}$$

where $g'(g'')$ is the reduced gravity parameter appropriate to the first (second) interface. Other notation is like that employed in the previous section (see Fig. 3) and for analytical convenience, we will again employ the Ekman pumping and topographic forms used in the previous section.

We assume here that the wind-driving is sufficiently strong that the second layer develops closed geostrophic contours and is thus set into motion. Parametrically, this requires:

$$x_e - \frac{\beta g' H_2}{f_o^2 \alpha} \frac{\beta H_1}{f_o} > x_w \tag{A.4}$$

which for $H_1 = 300$ m, $H_2 = 700$ m and $g' = .014$ m s^{-2} is easily met. As before, we assume that the comparable condition in the third layer is not met, and thus that the abyss will be stagnant aside from topographically closed zones.

The solution now proceeds in the classical way. Namely, (A.2) demonstrates that the

second layer is uniform in q_2 where it is not stagnant. Given this, we assume the placement of the topographic anomaly is entirely within the area of closed second layer geostrophic contours. This is done for convenience and is not unlike North Atlantic observations near the AP. Also, both the AP and the ZD are found near regions of strong, upper layer mean flows. Finally, although it is algebraically tedious, one can solve the cases where the topography is partially to wholly outside the homogenized q regions.

In regions where both deeper layers are at rest,

$$\psi_1 = \frac{f_o w_e (x - x_e)}{\beta H_1}. \tag{A.5}$$

In regions where the third layer is at rest, but q_2 is uniform,

$$\psi_1 = \left[\frac{f_o w_e (g' + g'')x}{\beta} - \frac{g' g'' H_2^2 \beta y}{f_o^2}\right]\left[\frac{1}{(g' + g'')H_1 + g'' H_2}\right] + C_1 \tag{A.6}$$

$$\psi_2 = \left(\frac{g'' f_o w_e x}{\beta} + \frac{\beta g' g'' H_1 H_2 y}{f_o^2}\right)\left(\frac{1}{(g'' + g')H_1 + g'' H_2}\right) + C_2 \tag{A.7}$$

where C_1 and C_2 are constants. Given h_b, the lower-layer potential vorticity, where $\psi_3 = 0$, is

$$q_3 = \frac{-f_o h_{bo}}{H_3 r_o^2}\left(\left(x - \frac{f_o^2 w_e r_o^2}{2h_{bo}\beta(g' H_1 + g''(H_1 + H_2))}\right)^2 + \left(y - \frac{r_o^2 \beta}{2 f_o h_{bo}} \frac{(g' H_1 (H_2 + H_3) + g'' (H_1 + H_2) H_3)}{g' H_1 + g''(H_1 + H_2)}\right)^2\right) + C_q \tag{A.8}$$

where C_q is constant. Hence if the point

$$\left(\frac{f_o^2 w_e r_o^2}{2h_{bo}\beta(g' H_1 + g''(H_1 + H_2))}, \frac{r_o^2 \beta}{2 f_o h_{bo}}\left(\frac{g' H_1 (H_2 + H_3) + g'' H_3 (H_1 + H_2)}{g' H_1 + g''(H_1 + H_2)}\right)\right)$$

lies within $x^2 + y^2 = r_o^2$, closed q_3 zones exist.

Inside such zones, according to (A.3):

$$q_3 = \frac{D}{R}\psi_3 + C_3 \tag{A.9}$$

where C_3 is a constant. Using (A.9) and the fact that q_2 is a constant then yields a relation between ψ_1 and ψ_2. Eq. (A.1) then returns

$$J(\psi_1, Q_1) = \frac{f_o w_e}{H_1} + R\nabla^2 q_1 \tag{A.10}$$

where

$$Q_1 = \frac{-g''f_o h_{bo}}{r_o^2 H_1 [g''(1+X) + g'X]} \cdot \left(x^2 + \left(y - \frac{\beta r_o^2}{2f_o h_{bo} g''} (g''H + X(g'' + g')H_1 + g''XH_2) \right)^2 \right) + C_{Q1} \tag{A.11}$$

C_{Q1} is a constant and $X = Dg''H_3/f_o^2 R$. The Q_1 contours in (A.11) take the form of circles, and a critical criteria for h_{bo} and D insuring the existence of closed Q_1 contours is easily obtained. For example, the algebraically convenient limit of small $X = Dg''H_3/R$ yields

$$Q_1 = C_{q1} - \frac{f_o h_{bo}}{H_1 r_o^2} \left(x^2 + \left(y - \frac{\beta r_o^2 H}{2f_o h_{bo}} \right)^2 \right) \tag{A.12}$$

and thus a critical condition

$$\frac{\beta H r_o}{2f_o h_{bo}} < 1 \tag{A.13}$$

identical to the condition for the existence of closed barotropic $f/(H - h_b)$ contours.

In the more realistic case of $Dg''H_3/Rf_o^2 = 1$, the criterion on h_{bo} reduces to:

$$h_{bo} > 330 \text{ m} \tag{A.14}$$

where we have used $H_1 = 300$ m, $H_2 = 700$ m, $H_3 = 4000$ m, $g' = .014$ m s^{-2} and $g'' = .007$ m s^{-2}. Clearly, the AP and the ZD both exceed this constraint. A plot of a shielded layer 3 region generated by topography appears in Figure 5 for these parameter settings and a Gaussian bump with $h_{bo} = 800$ m.

It is now a matter of straightforward, if tedious, algebra to compute the transports in each layer for the case of shielded layer 1. The results and the tendencies discussed in Section 2 are again resident in these solutions. The model schematic in Figure 3 shows the three layer dynamics, with Ekman mass fluxes balanced by eddy fluxes, and eventually, by bottom Ekman fluxes. The important result that transport is inversely proportional to bottom friction is found.

REFERENCES

Becker, J. 1995. An inertial model of the general circulation in an ocean with bottom topography, in Proceedings, 'Aha Huliko' a Hawaiian Winter Workshop, P. Muller and D. Henderson, eds., 125–130.

Blumsack, S. and G. Weatherly. 1989. Observations of the nearby flow and a model for the growth of mudwaves. Deep-Sea Res., 36, 1327–1339.

Cessi, P. and J. Pedlosky. 1986. On the role of topography in the ocean circulation. J. Mar. Res., 44, 445–471.

Danabasaglu, G., J. C. McWilliams and P. R. Gent. 1994. The role of mesoscale tracer transports in the global ocean circulation. Science, 264, 1123–1126.

De Szoeke, R. 1985. Wind-driven mid-ocean baroclinic gyres over topography: a circulation equation extending the Sverdrup relation. J. Mar. Res., 43, 793–824.

Flood, R. and A. Shor. 1988. Project Mudwaves: a coordinated study of abyssal bedforms and sedimentation in the Argentine Basin. Trans. Amer. Geophys. Union, 69, 1258.

Gent, P. R. and J. C. McWilliams. 1990. Isopycnal mixing in ocean circulation models. J. Phys. Oceanogr., 20, 150–155.

Holland, W. 1978. The role of mesoscale eddies in the general circulation of the ocean-numerical experiments using a wind-driven quasi-geostrophic model. J. Phys. Oceanogr., 8, 363–392.

Holloway, G. 1992. Representing topographic stress for large-scale ocean models. J. Phys. Oceanogr., 22, 1033–1046.

Kawase, M. 1993. Effects of a concave bottom geometry on the upwelling-driven circulation in an abyssal ocean basin. J. Phys. Oceanogr., 23, 400–405.

Kawase, M. and D. Straub. 1991. Spinup of source-driven circulation in an abyssal basin in the presence of bottom topography. J. Phys. Oceanogr., 21, 1501–1514.

Klein, B. and G. Seidler. 1989. On the origin of the Azores Current. J. Geophys. Res., 94, 6159–6168.

Koblinsky, J. C. 1990. The global distribution of f/H and the barotropic response of the ocean. J. Geophys. Res., 3, 3213–3218.

Kraus, W. and R. Kase. 1984. Mean circulation and eddy kinetic energy in the eastern North Atlantic. J. Geophys. Res., 89, 3407–3415.

Leetmaa, A., P. Niiler and H. Stommel. 1977. Does the Sverdrup relation account for the mid-Atlantic circulation? J. Mar. Res., 35, 1–10.

Lozier, M., W. Owens and R. Curry. 1995. The climatology of the North Atlantic. Prog. Oceanogr., 36, 1–44.

Luyten, J. R., J. Pedlosky and H. Stommel. 1983. The ventilated thermocline. J. Phys. Oceanogr., 13, 292–309.

Marshall, D. 1995a. Influence of topography on the large-scale ocean circulation. J. Phys. Oceanogr., 25, 1622–1635.

—— 1995b. Topographic steering of the Antarctic Circumpolar Current. J. Phys. Oceanogr., 25, 1636–1650.

McDowell, S., P. Rhines and T. Keffer. 1982. North Atlantic potential vorticity and its relation to the general circulation. J. Phys. Oceanogr., 12, 1417–1436.

Pollard, R., M. Griffiths, S. Cunningham, J. Read, F. Perez and A. Rios. 1996. Vivaldi, 1991: A study of the formation, circulation and ventilation of Eastern North Atlantic Central Water. Prog. Oceanogr., 37, 167–192.

Rhines, P. B. 1989. Deep planetary circulation and topography: simple models of midocean flows. J. Phys. Oceanogr., 19, 1449–1470.

Rhines, P. B. and W. Young. 1982a. Homogenization of potential vorticity in planetary gyres. J. Fluid Mech., 122, 347–367.

—— 1982b. A theory of the wind-driven circulation, I. Mid-ocean gyres. J. Mar. Res., 40 (Suppl), 559–596.

Salmon, R. 1992. A two-layer Gulf Stream over a continental slope. J. Mar. Res., 52, 865–908.

Saunders, P. and B. King. 1995a. Bottom currents derived from a shipborne ADCP on WOCE cruise A11 in the South Atlantic. J. Phys. Oceanogr., 25, 329–347.

—— 1995b. Ocean fluxes on the WOCE A11 Section. J. Phys. Oceanogr., 25, 1942–1958.

Sverdrup, H. 1947. Wind-driven currents in a baroclinic ocean; with application to the equatorial currents of the eastern Pacific. Proc. Natl. Acad. Sci., USA, 33, 318–326.

Sy, A. 1988. Investigation of large-scale circulation patterns in the central North Atlantic: The North Atlantic Current, the Azores Current, and the Mediterranean Water Plume in the area of the Mid-Atlantic Ridge. Deep-Sea Res., 35, 383–413.

Thompson, L. 1995. The effect of continental rises on the wind-driven ocean circulation. J. Phys. Oceanogr., 25, 1296–1316.

Weatherly, G. 1984. An estimate of bottom frictional dissipation by Gulf Stream fluctuations. J. Mar. Res., 42, 289–301.

—— 1993. On deep-current and hydrographic observations from a mudwave region and elsewhere in the Argentine Basin. Deep-Sea Res., 40, 939–961.

Welander, P. 1968. Wind-driven circulation in one- and two-layer oceans of variable depth. Tellus, 20, 1–15.

Wunsch, C. and A. Roemmich. 1985. Is the North Atlantic in Sverdrup balance? J. Phys. Oceanogr., 15, 1876–1880.

Young, W. 1981. The vertical structure of the wind-driven circulation, MIT-WHOI PH.D. Dissertation, WHOI Technical Report #WHOI-81-89, 215 pp.

Received: 4 March, 1997; revised: 11 November, 1997.